

Elastic Lattice Enabling Reversible Tetrahedral Li Storage Sites in a High-Capacity Manganese Oxide Cathode

Weiyuan Huang, Luyi Yang, Zhefeng Chen, Tongchao Liu, Guoxi Ren, Peizhao Shan, Bin-Wei Zhang, Shiming Chen, Shunning Li, Jianyuan Li, Cong Lin, Wenguang Zhao, Jimin Qiu, Jianjun Fang, Mingjian Zhang, Cheng Dong, Fan Li, Yong Yang, Cheng-Jun Sun, Yang Ren, Qingzhen Huang, Guangjin Hou, Shi-Xue Dou, Jun Lu, Khalil Amine, and Feng Pan*

The key to breaking through the capacity limitation imposed by intercalation chemistry lies in the ability to harness more active sites that can reversibly accommodate more ions (e.g., Li⁺) and electrons within a finite space. However, excessive Li-ion insertion into the Li layer of layered cathodes results in fast performance decay due to the huge lattice change and irreversible phase transformation. In this study, an ultrahigh reversible capacity is demonstrated by a layered oxide cathode purely based on manganese. Through a wealth of characterizations, it is clarified that the presence of low-content Li₂MnO₃ domains not only reduces the amount of irreversible O loss; but also regulates Mn migration in LiMnO2 domains, enabling elastic lattice with high reversibility for tetrahedral sites Li-ion storage in Li layers. This work utilizes bulk cation disorder to create stable Li-ion-storage tetrahedral sites and an elastic lattice for layered materials, with a reversible capacity of 600 mA h g^{-1} , demonstrated in th range 0.6–4.9 V versus Li/Li⁺ at 10 mA g⁻¹. Admittedly, discharging to 0.6 V might be too low for practical use, but this exploration is still of great importance as it conceptually demonstrates the limit of Li-ions insertion into layered oxide materials.

1. Introduction

The ever-increasing demand for better and more sustainable energy storage systems relies on the discovery of positive electrode materials for lithium-ion batteries (LIBs) with high energy density, long cycle life, and low costs.^[1–4] One promising approach to achieve such target is to break through the current capacity limits imposed by intercalation chemistries adopted in stateof-the-art LIBs via activating new storage mechanisms within a limited framework, so that extra Li+ could be accommodated. Extending the operating potential window to allow extra Li+ insertion into the cathode material is an effective approach for high capacity. Previous studies have shown that extra Li+ can be inserted into tetrahedron sites of the layered LiNiO2

W. Huang, L. Yang, Z. Chen, S. Chen, S. Li, J. Li, C. Lin, W. Zhao, J. Qiu, J. Fang, M. Zhang, C. Dong, F. Pan School of Advanced Materials

Peking University Shenzhen Graduate School

Shenzhen 518055, P. R. China E-mail: panfeng@pkusz.edu.cn T. Liu, C.-J. Sun, J. Lu, K. Amine

Chemical Sciences and Engineering Division

Argonne National Laboratory Lemont, IL 60439, USA

State Key Laboratory of Functional Materials for Informatics Shanghai Institute of Microsystem and Information Technology Chinese Academy of Sciences

Shanghai 200050, P. R. China

P. Shan, Y. Yang

State Key Laboratory for Physical Chemistry of Solid Surfaces and Department of Chemistry

College of Chemistry and Chemical Engineering

Xiamen University

Xiamen 361005, P. R. China



The ORCID identification number(s) for the author(s) of this article can be found under https://doi.org/10.1002/adma.202202745.

DOI: 10.1002/adma.202202745

B.-W. Zhang, S.-X. Dou Institute for Superconducting and Electronic Materials University of Wollongong Wollongong, New South Wales 2522, Australia F. Li, G. Hou

State Key Laboratory of Catalysis Dalian Institute of Chemical Physics Chinese Academy of Sciences Dalian, Liaoning Province 116023, P. R. China

University of Chinese Academy of Sciences Beijing 100049, P. R. China

X-Ray Science Division Argonne National Laboratory Lemont, IL 60439, USA

Q. Huang

NIST Center for Neutron Research

National Institute of Standards and Technology 100 Bureau Drive, Gaithersburg, MD 20899, USA

Material Science and Engineering

Stanford University Stanford, CA 94305, USA

15214095, 2022, 30, Downloaded from https://advanced.on/initibitrary.wiley.com/doi/10.1002/adm.202202745 by University Town Of Shenzhen, Wiley Online Library on [23/11/2025]. See the Terms and Conditions (https://onlinelbitrary.wiley.com/terms-and-conditions) on Wiley Online Library or rules of use; OA articles are governed by the applicable Creative Commons Licensea

framework under deep discharge state to form Li_2NiO_2 structure. [5,6] However, this process causes irreversible phase transition from O3 structure (oxygen stacking in ABCABC sequence) to 1T structure (oxygen stacking in ABAB sequence), hence the fast capacity decay. [7,8]

Due to the limited global Co and Ni reserve and the associated supply chain risks, Li- and Mn-rich (LMR) layered oxides have attracted worldwide attention as a promising positive electrode material for next-gen sustainable batteries.[9-13] The discovery of anionic redox chemistry (i.e., $2O^{2-} - (4-n)e^- \rightarrow O_2^{n-}$) led to a new paradigm to opening up new redox centers for extra Li⁺ storage in the transitional metal (TM) layer.^[14–16] Recent studies found that pure Li₂MnO₃ phase actually does not offer any reversible oxygen redox activities.[17,18] The oxygen activities could be modulated toward reversible reactions when the system is dragged away from the Li₂MnO₃ system. Therefore, significant efforts have been made to fully tap the potential held by lithium-manganese oxide (Li-Mn-O) cathode materials. For instance, O3-type layered Li_{0.6}[Li_{0.2}Mn_{0.8}]O₂^[19] and Li_{0.700}[Li_{0.222}Mn_{0.756}]O₂^[20] both exhibit intralayer Li/Mn disordering in Mn layers (confirmed by the missing superlattice peaks). O2-type layered Li_{0.78}[Li_{0.24}Mn_{0.76}]O₂^[21] was also reported to exhibit a structure with 0.72 Li@Mn₆ (i.e., superstructure unit with one Li atom surround by a hexagonal ring consisting of six Mn atoms in TM layers^[22–24]) and 0.28 Mn@Mn₆ ordering in Mn layers (calculated based on its fully lithiated state of Li[Li_{0.24}Mn_{0.76}]O₂, corresponding to 0.63Li₂MnO₃·0.37LiMnO₂). Despite delivering high initial specific capacities, these layered LMR materials suffer from severe performance degradation during cycling. In addition, Li₄Mn₂O₅, [25] Li₂MnO₃-LiMn₂O₄ composite, [26] and a series of fluorinated Li-Mn-O materials[15,27-29] have been investigated in a wide operating potential window to accommodate more Li-ion and achieve a high capacity >300 mA h g⁻¹. However, the cycling stability of abovementioned rock-salt materials is still unsatisfactory, which can be generally attributed to the adverse nature of rock-salt structure and irreversible structural evolution during cycling. In $\text{Li}_{1,2}\text{Ni}_{0,13}\text{Mn}_{0,54}\text{Co}_{0,13}\text{O}_2^{[30]}$ and $\text{Li}_{1,2}\text{Cr}_{0,4}\text{Mn}_{0,4}\text{O}_2^{[31]}$ and Li_{1,2}Ru_{0,5}Mn_{0,5}O₂^[32] cathodes, such phase transition behavior from O3 to 1T was effectively suppressed due to the migration Mn or Cr ions to Li-slabs, which serve as "supporting pillars" to stabilize the structure with Li+ occupied tetrahedral sites. Nevertheless, the huge lattice changes upon repeated cycling still induce particle cracking, which generally leads to performance deterioration.

Herein, we reported a new O3-type layered oxide cathode based purely on manganese, Li_{0.83}Mn_{0.84}O₂ (LMO), which consist of 0.48 Li@Mn₆ ordering and 0.52 Mn@Mn₆ structure units in Mn layers (detailed calculation method is demonstrated in Experimental Section). For the first time we operated the LMO cathode at deep discharge state and achieved breakthroughs in both capacity and stability. Through a wealth of characterizations, it is revealed that the reconstructed structure consists of abundant of misplaced Mn-ions acting as structural support for an elastic Mn layer, which not only enables extra Li⁺ storage in the tetrahedral sites of Li layer rather than the conventional octahedral sites, but also tolerates layer distortion to maintain structural integrity during repeated cycling. The presence of low-content Li₂MnO₃ domains not only reduces

the amount of irreversible O loss in pure Li_2MnO_3 phase, but also regulates Mn migration in LiMnO_2 domains. [33,34] As a result, an unprecedented reversible capacity of \approx 412 mA h g⁻¹ (1.3–4.9 V) and even >600 mA h g⁻¹ (0.6–4.9 V) can be achieved under a wide operation potential window. Through reversibly accessing the hitherto unavailable Li storage sites in layered Li–Mn–O based materials, this work provides a new perspective on achieving high-capacity cathodes.

2. Results and Discussion

2.1. Structural Characterization of Pristine LMO

The pristine LMO material is obtained via ion exchange method from a sodium-based precursor (see details in Experimental Section). The Rietveld refinement results show the prepared sodic precursor is a P3-type sodic layered oxide with minor lithiated phase, exhibiting R3m space group (Figure S1, Supporting Information). The weight ratio of sodic phase and lithiated phase is about 0.88:0.12. The detailed lattice parameters and structure parameters are displayed in Tables S1-S3, Supporting Information. The molecular formula of LMO is determined to be Li_{0.83}Mn_{0.84}O₂ using inductively coupled plasma-atomic emission spectroscopy (ICP-AES, see details in Table S4, Supporting Information). Both scanning electron microscope (SEM) and transmission electron microscope (TEM) images (Figure S2, Supporting Information) indicate that the obtained material consists of micro-sized secondary particles and nanosized primary particles. Powder X-ray diffraction (XRD) and neutron powder diffraction (NPD) have been jointly employed to determine the crystalline structure of LMO (Figure 1a,b) as neutron scattering lengths are independent of electron numbers and thus enabling high sensitivity of light elements (e.g., Li).[35] The corresponding Rietveld refinements of LMO were performed, revealing a layered structure with $R\overline{3}m$ space group. The detailed refined lattice parameters and structure parameters are listed in Tables S5 and S6, Supporting Information. It can be found there are 0.16 Li and 0.84 Mn in the TM layer (3a sites) and 0.67 Li in the Li layer (3b sites). In addition, an unindexed peak at 20.9° can be identified as superlattice peak, which can be related to the Li@Mn₆ ordering in TM layers.^[22-24]

Additionally, continuous rotation electron diffraction (cRED) is used to detect submicron/nanometer-scale crystal structure of LMO. The 3D reciprocal lattice data were obtained by combining the collected electron diffraction data from a LMO single particle during rotation (Figure 1c). The corresponding reciprocal lattice data projected to a*b* (Figure 1d), a*c* (Figure 1e), and b*c* (Figure 1f) planes are also recorded for observation. The obtained cRED data can be well fitted to the unit cell of $R\overline{3}$ m space group, and the discrete and clear reflection spots along a^* , b^* , and c^* axes indicate the absence of obvious structural defects in pristine LMO, revealing high crystallinity of LMO with flat layered structure. [36] To investigate the local structure of LMO, high resolution TEM (HRTEM, Figure S3, Supporting Information) and high angle annular dark field scanning transmission electron microscopy (HAADF-STEM) technique were employed (Figure 1g,h). Since only Mn atoms can be visualized in the HAADF image, the observed Mn-Mn "dumbbells" can

15214095, 2022, 30, Downloaded from https://advancec

.com/doi/10.1002/adma.202202745 by University Town Of Shenzhen, Wiley Online Library on [23/11/2025]. See the Terms

and-conditions) on Wiley Online Library for rules of use; OA articles are governed by the applicable Creative Commons

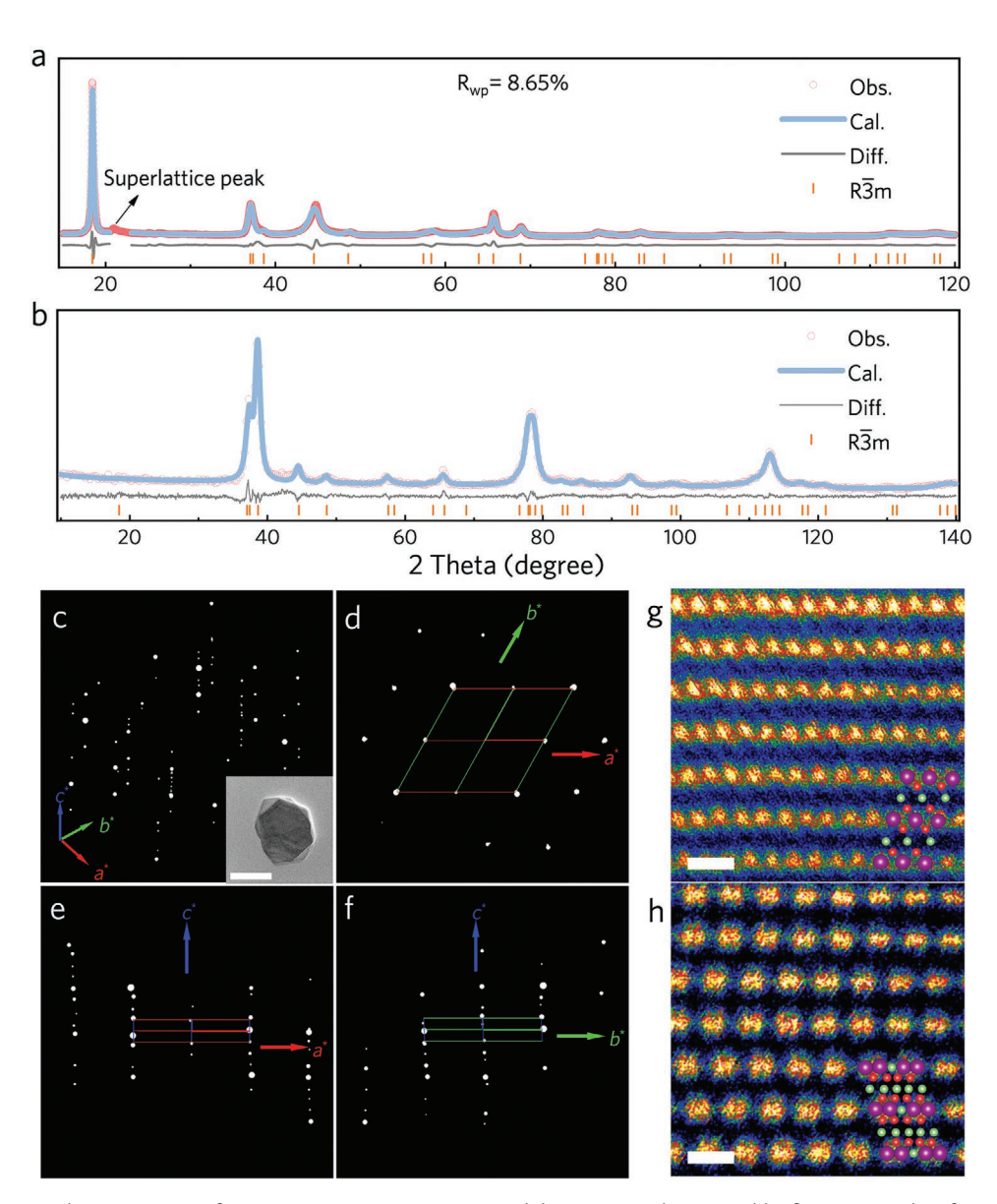


Figure 1. The structure characterization of pristine LMO. a) XRD patterns and the corresponding Rietveld refinement results of pristine LMO. b) PND patterns and the corresponding Rietveld refinement results of pristine LMO. c) Overall 3D reciprocal lattice of the selected LMO particle. Inset (scale bar 100 nm) is the corresponding particle for cRED. d-f) Reciprocal lattice pattern viewed along e^{-x} -axis, e^{-x} -axis, and e^{-x} -axis, respectively. g,h) HAADF images of the pristine LMO with different structured nanodomains, scale bar = 0.5 nm. Colored spheres represent proposed atom arrangements of Mn (purple), Li (green), and O (red).

be associated with honeycomb Mn_6 -ring ordering in TM layers (nether panel in Figure 1h, intensity lines shown in Figure S4, Supporting Information), which is consistent with the superlattice peak (i.e., $\text{Li}@Mn_6$ ordering in TM layer) in Figure 1a. The multi-scale characterizations above demonstrate that LiMnO_2 and Li_2MnO_3 -like structure domains coexist in pristine LMO.

2.2. Electrochemical Performance of LMO

Galvanostatic cycling is carried out to evaluate the electrochemical performance of LMO. Under a low specific current density, the first-cycle charge and discharge capacities are 274 and 412 mA h g⁻¹ (\approx 1166.8 Wh kg⁻¹, calculated based the mass of active material), respectively (**Figure 2a**), the corresponding dQ/dV and cyclic voltammogram (CV) curves are displayed in Figure S5, Supporting Information. This capacity discrepancy is attributed to the Li-deficient nature of the pristine LMO, and a much higher coulombic efficiency can be achieved during the following cycle. As shown in Figure S6, Supporting Information, LMO can still deliver a high discharge capacity of \approx 346.7 mA h g⁻¹ after 30 cycles under a specific current of 10 mA g⁻¹. Furthermore, a discharge capacity of \approx 337.2 mA h g⁻¹ with high specific energy retention (97.2%), capacity retention (98.2%), and average coulombic efficiency (96.8%) can be achieved after 50 cycles (Figure 2b and Figure S7, Supporting

www.advancedsciencenews.com

1521495,2022, 30, Downloaded from https://dram.ed online library.wiley.com/doi/10.1002adma.020202745 by University Town Of Shenzhen, Wiley Online Library on [23/11/2025]. See the Terms and Conditions (https://onlinelibrary.wiley.com/terms-and-conditions) on Wiley Online Library for rules of use; OA archies are governed by the applicable Centwise Commons I

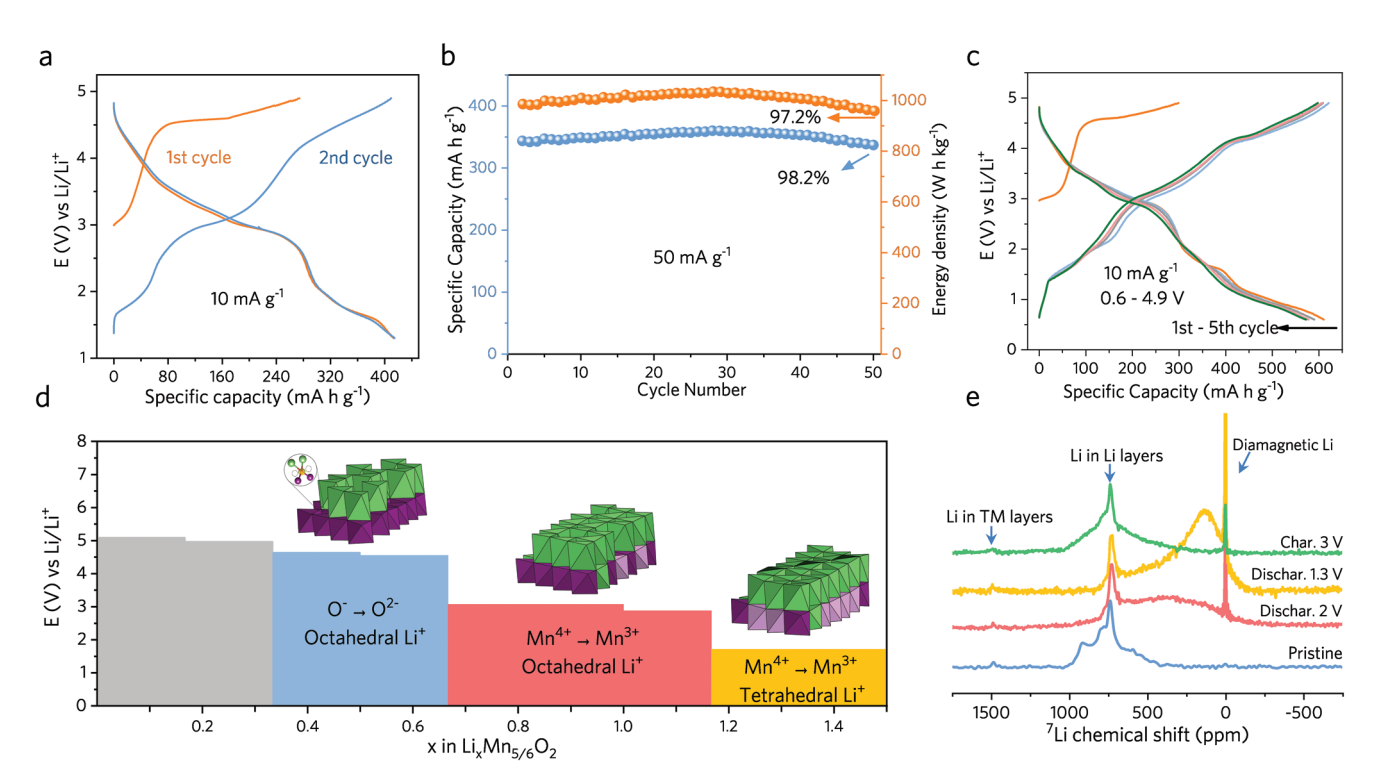


Figure 2. High capacity of LMO and its origin. a) Voltage profiles of the first two cycles (specific current density: 10 mA g⁻¹). b) Variation of specific discharge capacity and energy density with cycle number (specific current density: 50 mA g⁻¹). c) Voltage profiles of the initial five cycle process (cut-off voltage: 0.6-4.9 V versus Li/Li⁺, specific current density: 10 mA g⁻¹). d) Simulated discharge plateaus and the corresponding redox pairs according to pristine LMO (using Li_xMn_{5/6}O₂) at various degrees of discharge between 4.9 and 1.3 V. e, ex situ ⁷Li ssNMR spectra of pristine LMO powder, electrodes discharged to 2 V, 1.3 V, and recharged to 3 V.

Information), corresponding to an average voltage retention of 98.9%, which is comparable with other previously reported LMR materials (see detailed comparisons in Table S7, Supporting Information). Under an elevated specific current of 200 mA g⁻¹, an initial capacity of 266 mA h g⁻¹ can be obtained with a mass loading of 3 mg cm⁻². After 150 cycles, high capacity (87.0%), average coulombic efficiency (96.1%), and average discharge voltage (98.5%) retention can be achieved, respectively (Figures S8 and S9a, Supporting Information). After increasing the loading of LMO to ≈8 mg cm⁻², high specific capacity of \approx 350 mAh g⁻¹ and \approx 270 mAh g⁻¹ can still be obtained at 50 and $200~\text{mA}~\text{g}^{-1}$, respectively. Since most LMR materials suffer from poor rate performance due to slow kinetics, their galvanostatic cycling tests were generally carried out under impractically low specific currents. Herein, the rate capability of LMO is also tested under various C-rates (Figure S10, Supporting Information, where 1 C corresponds to the specific current density of 400 mA g⁻¹). LMO exhibits a specific capacity of 151 mA h g⁻¹ at 5 C, which greatly extends its application scenarios. Due to the Li-deficiency in LMO, Li compensation is necessary for its potential use in practical batteries. Therefore, a proof-of-concept pouch cell is assembled by coupling LMO with a graphite anode, which was chemically prelithiated according to a previously reported method.^[37] Under 50 mA g⁻¹, the full cell exhibits an initial capacity of 348 mA h g⁻¹ at 50 mA g⁻¹, with retention of 95.1% after 20 cycles (Figure S11, Supporting Information).

Generally, extending the lower cut-off voltage during discharging allows extra Li+ insertion to obtain a higher practical capacity. Nevertheless, over-discharging layered oxide cathodes to excessively low voltages would lead to battery failure as extra Li⁺ squeezed into neighboring tetrahedral sites from octahedral sites is generally accompanied with the structural collapse. [38,39] For LMO synthesized in this work, however, shifting the lower cut off voltage to 0.6 V versus Li/Li+ makes an ultrahigh capacity of 610 mA h g⁻¹ (≈1368.6 Wh kg⁻¹) accessible reversibly (Figure 2c), which is far beyond any reported values so far. More importantly, the capacity and average voltage barely changed after five cycles. Compared with the result obtained in the voltage range of 1.3-4.9 V, the charge capacity above 4 V region is much higher when tested under 0.6-4.9 V. Similar phenomena can also be found in many previous studies, [6,30,32] which could be explained by the retarded Li+ intercalation/ deintercalation kinetics under a higher tetrahedral Li+ occupation, hence the large voltage hysteresis. At 50 mA g⁻¹, an initial capacity of 465 mA h g⁻¹ can be also achieved with capacity retention of 84% after 20 cycles (Figure S12, Supporting Information). Admittedly, discharging to 0.6 V versus Li/Li⁺ might be too low for practical use, this exploration is still of great importance as it conceptually demonstrates the limit of Li+ insertion into layered oxide materials since in a real battery, cathode particles in some local areas will be inevitably over-discharged due to polarization. The highly stable structures of LMO ensures its cycle reversibility under extreme testing conditions. Firstprinciple simulations is carried out to estimate the redox center and Li occupation in LMO (denoted as LixMn5/6O2). By obtaining the convex hull curve of formation energy of all

1521405, 2022, 30, Downloaded from https://alvanced.onlinibibrary.wiley.com/doi/10.1002/adma.02202745 by University Town Of Shanzhen, Wiley Online Library on [23/11/2025]. See the Terms and Conditions (https://onlinelibrary.wiley.com/etms-and-conditions) on Wiley Online Library for rules of use; OA articles are governed by the applicable Centwive Commons In 15/14/2025. See the Terms and Conditions of the Terms and Conditions on Wiley Online Library for rules of use; OA articles are governed by the applicable Centwive Commons In 15/14/2025. See the Terms and Conditions of the Terms an

possible configurations (Figure S13, Supporting Information), stable intermediate configurations are confirmed. According to the computational result (Figure 2d), the first two discharge plateaus (≈4.6 V, ≈3.0 V versus Li/Li+) are attributed to anion and Mn reduction (Mn⁴⁺ + $e^- \rightarrow$ Mn³⁺), respectively, while Li⁺ inserts into octahedral sites in Li slabs to form LiO₆ octahedra. For the plateau at ≈1.6 versus Li/Li+, although Mn is still electrochemically active as a redox center, octahedral sites in Li-slabs cannot accommodate any more Li+. Therefore, Li+ starts to insert neighboring tetrahedral sites in Li-slabs instead of octahedral ones.[40] Moreover, computational results indicate that at the end of this plateau, Mn³⁺ remains relatively stable against disproportionation (Figure S14, Supporting Information). This simulation is experimentally verified by ⁷Li solid-state nuclear magnetic resonance (ssNMR) spectra (Figure 2e and Figure S15a, Supporting Information). The small peak around ≈1490 ppm represents Li+ in transition metal layer (Li_{TM}), corresponding to the superlattice structure in pristine LMO; whereas the broad band at ≈740 ppm reflects the chemical environment of Li⁺ in Li-slabs.^[41] In addition, the peak at 0 ppm arises from the Li⁺ in diamagnetic environments (e.g., residual electrolyte salt or electrolyte decomposition species). When discharged to 2 V, a new broad peak appeared around 400-500 ppm (see enlarged spectra in Figure S15b, Supporting Information), which is consistent with Li⁺ occupation in tetrahedral sites of Li layers reported in previous studies.^[41,42] As Li⁺ continuously inserted into the cathode, a resonance peak at much lower chemical shift (136 ppm) can be observed at 1.3 V. Such peak shift might arise from Li⁺ between distorted Mn layers^[43] as well as the occupation of tetrahedral sites in Li-slabs. [44] As subsequently recharged to 3 V, the broad peaks at low chemical shift (400-500 ppm and 136 ppm) disappeared while the original peaks at ≈740 ppm and ≈1490 ppm still exist, indicates a reversible structural evolution process in LMO during cycling.

Despite the much-improved cycling reversibility, inevitable capacity and voltage decay during long-term cycling can still be observed. This can be related to the structure transformations of LMO, including layer-spinel phase transformation, the decrease of interlayer spacing and crystallinity, as well as the structure defect formation (Figures S16 and S17, Supporting Information). For comparison, layered Li_{0.7}MnO₂ suffered from severe structure deterioration from original layered phase to spinel-like phase and distorted spinel phase after 10 and 50 cycles, respectively (Figure S18, Supporting Information). In addition, Mn dissolution (Figure S19, Supporting Information) and the possible side reactions with the electrolyte (Figure S20, Supporting Information) also can be found in the cycled LMO cathode. To further improve the electrochemical performance, future studies should focus on surface protection and electrolyte optimization strategies.

2.3. Reversible Structural Evolution

In situ synchrotron XRD is first employed to monitor the phase evolution process of pristine LMO during cycling (**Figure 3**a). Upon initial charging, the (003) peak around 1.4° shifts toward higher angle, indicating a reduced interlayer distance due to Li⁺ deintercalation; upon discharging, the (003) peak shifts back to

lower angle along with lithiation process. This variation tendency of interlayer distance (see detailed data in Figure S21, Supporting Information) is opposite to the behavior of traditional layered oxides that involves the redox reaction of TM cations only,[36] implying anionic redox dominated reactions as anionic oxidation leads to decreased repulsion force between to neighboring oxygen layers, hence a reduced interlayer distance.[19,45] It should be also noted that the peak shift became more drastic when discharged to 2 V versus Li/Li+, which could be attributed to the dramatically enlarged interlayer spacing caused by extra Li⁺ occupation in tetrahedral sites. Therefore, in the subsequent charging process, the interlayer spacing reduces as Li+ being extracted from the tetrahedral sites, and the (003) peak shifts toward higher angle. In addition, O K-edge X-ray absorption spectroscopy (XAS) was carried out under total fluorescence yield (TFY, Figure 3b) and total electron yield (TEY, Figure S22, Supporting Information) modes. For pristine LMO, pre-edged peaks (<535 eV) in both spectra can be assigned to the transition of O 1s to the unoccupied states of O 2p orbitals hybridized with Mn 3d orbital. Upon charging, the formation of a shoulder feature at ≈530.5 eV infers the oxidized state of O.[19,46] Lattice oxidized oxygen species can be also observed from the ex situ X-ray photoeletron spectra (XPS) of O during charging (Figure S23, Supporting Information). The results of differential electrochemical mass spectroscopy (DEMS, Figure 3c) also show that the first charging process is accompanied by a small amount of O2 gas release, and there is no detectable O2 gas release in the subsequently cycles for LMO, indicating a stable structure has been formed after the first cycle. Furthermore, reversible peak shifting can be observed for other major XRD peaks while no new peak has emerged (Figure S24, Supporting Information). The well-maintained structural integrity of LMO explains its cycling stability.

Next, from the in situ Mn K-edge X-ray absorption nearedge structure (XANES) spectra (Figure 3d and Figure S25, Supporting Information), it can be observed that before being discharged to 2.8 V versus Li/Li+, the valence state of Mn in LMO increased and decreased slightly during charging and discharging, respectively. This result indicates that during this process, the redox reactions of both Mn and anion jointly contribute to the capacity. It is noteworthy that as the cell being discharged below 2.8 V versus Li/Li+, significant Mn reduction can be observed. This result, as well as the ex situ XPS (Figure S26, Supporting Information) have supported the theoretical hypothesis in Figure 2g that the accommodation of Li+ depends on Mn reduction at low voltages (<2.8 V versus Li/Li⁺). The Fourier transform of the Mn K-edge extended X-ray absorption fine structure (EXAFS) spectra (Figure 3e and Figure S27, Supporting Information) shows that the distance between Mn and its nearest neighboring O also become larger below 2.8 V versus Li/Li+, which could be attributed to the Jahn-Teller effect or the weakened electrostatic attraction between Mn-ion and O^{2–}; while for similar reasons, intraslab Mn-ions become closer.

2.4. Origin of Elastic Lattice on Atomistic Level

HAADF-STEM and cRED are jointly employed to probe the local atomic evolutions in LMO during cycling. The

1521495,2022, 30, Downloaded from https://dram.ed online library.wiley.com/doi/10.1002adma.020202745 by University Town Of Shenzhen, Wiley Online Library on [23/11/2025]. See the Terms and Conditions (https://onlinelibrary.wiley.com/terms-and-conditions) on Wiley Online Library for rules of use; OA archies are governed by the applicable Centwise Commons I

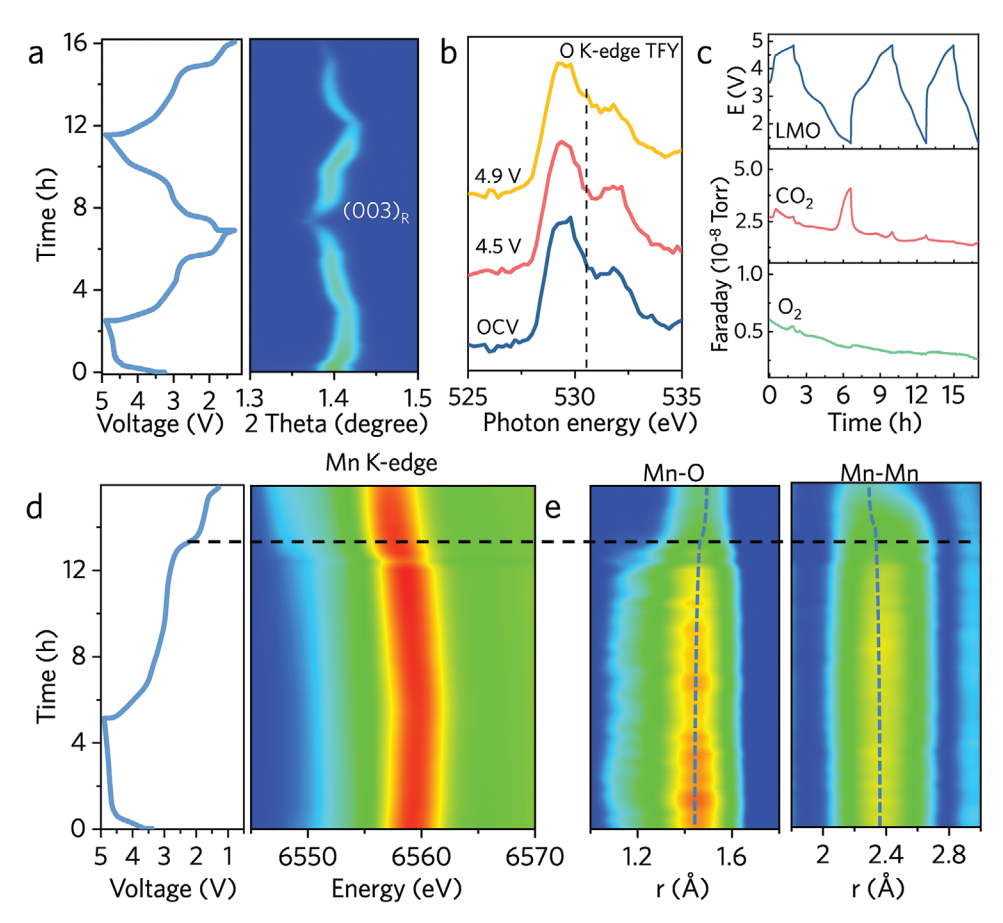


Figure 3. Structure evolution of pristine LMO. a) Contour plot of in situ synchrotron XRD patterns with selected angle regions during initial two cycles (cut-off voltage: 1.3–4.9 V versus Li/Li⁺, specific current density: 70 mA g⁻¹). b) TFY mode of O pre-edge region K-edge XAS spectra of LMO measured under different voltages. c) In situ DEMS measurement records gas release during cycling for LMO. d) Contour plot of in situ Mn K-edge XANES spectra during cycling. e) Fourier transform of the Mn K-edge extended EXAFS spectra, which represents the distance between Mn–O and Mn–Mn. Electrochemical testing condition for (d) and (e) is set between 1.3 and 4.9 V versus Li/Li⁺ with a specific current density of 30 mA g⁻¹.

HAADF-STEM image shows that after first charging to 4.9 V versus Li/Li+, Mn can be observed in Li layers (as marked in Figure 4a, line intensity is presented in Figure S28a,d, Supporting Information), forming Li/Mn antisites, while the discrete reciprocal lattice spots in cRED patterns of a single charged particle (Figure 4b-e) also confirm that the layered structure with flat Mn slabs is well-preserved after charging. However, when discharged to 1.3 V versus Li/Li⁺, flat Mn layers become curved and dislocated with additional Li+ insertion (Figure 4f). It should be noted that a larger number of Mn-ions can be observed in Li layers at discharged state (as marked in Figure 4f and Figure S28b,e, Supporting Information), which can be related to Mn3+ formation at low discharge voltage. Differing from the reported Li-rich manganese oxides, where Mn migration to Li-slabs mainly occur at the surface after the initial cycle,[10,47] LMO shows significant cation disorder in the bulk. This might be related to the relatively high content of LiMnO2-like layered structure in LMO, which is thermodynamically favorable for Mn migration to Li layers.[33,34,48] The streaked cRED reciprocal lattice spots (Figure 4g-i) along the c*-axis are consistent with HAADF-STEM image, revealing a rippled structure which is commonly observed in 2D materials owing to the high interlayer/intralayer stress. [49,50] Similar

phenomena in layered oxides have been considered detrimental to the cycling stability because high curvatures generally leads to structure collapse. [36,51] However, as pristine LMO recharged to 3 V versus Li/Li+, both HAADF-STEM image (Figure 4k) and cRED (Figure 41-o) patterns have indicated that the flatness of Mn slabs is restored. Meanwhile, the previously formed Li/Mn antisites after the first cycle charging remain existent during the sequential electrochemical steps (as marked in Figure 4k and Figure S28c,f, Supporting Information). It should be noted that due to the Jahn-Teller effect of Mn³⁺, severe Li-Mn interchange tends to occur in LiMnO2 domains upon discharging, eventually resulting in electrochemically inactive rock-salt structures.[33,34] For LMO, the existence of Li₂MnO₃ domains not only mitigate Jahn–Teller effect by increasing the average valence state of Mn, but also serve as a buffer to prevent irreversible phase changes, hence the active material is well-maintained.

According to the computational results (Figure 4p), excess Li⁺ could be either evenly distributed in Li-slabs or enriched in a limited locality, depending on the existence of Li/Mn antisites. The former tends to undergo a phase transition into O1-type structure whereas the O3 phase could be stabilized for the latter case. Owing to the high stress generated by excess lithiation in tetrahedral sites, the later configuration

15214095, 2022. 30, Downloaded from https://advanced.onlinelbrary.wiley.com/doi/10.1002/adma.202202745 by University Town Of Shenzhen, Wiley Online Library on [23/11/2025]. See the Terms and Conditions (https://onlinelbrary.wiley

inditions) on Wiley Online Library for rules of use; OA articles are governed by the applicable Creative Commons

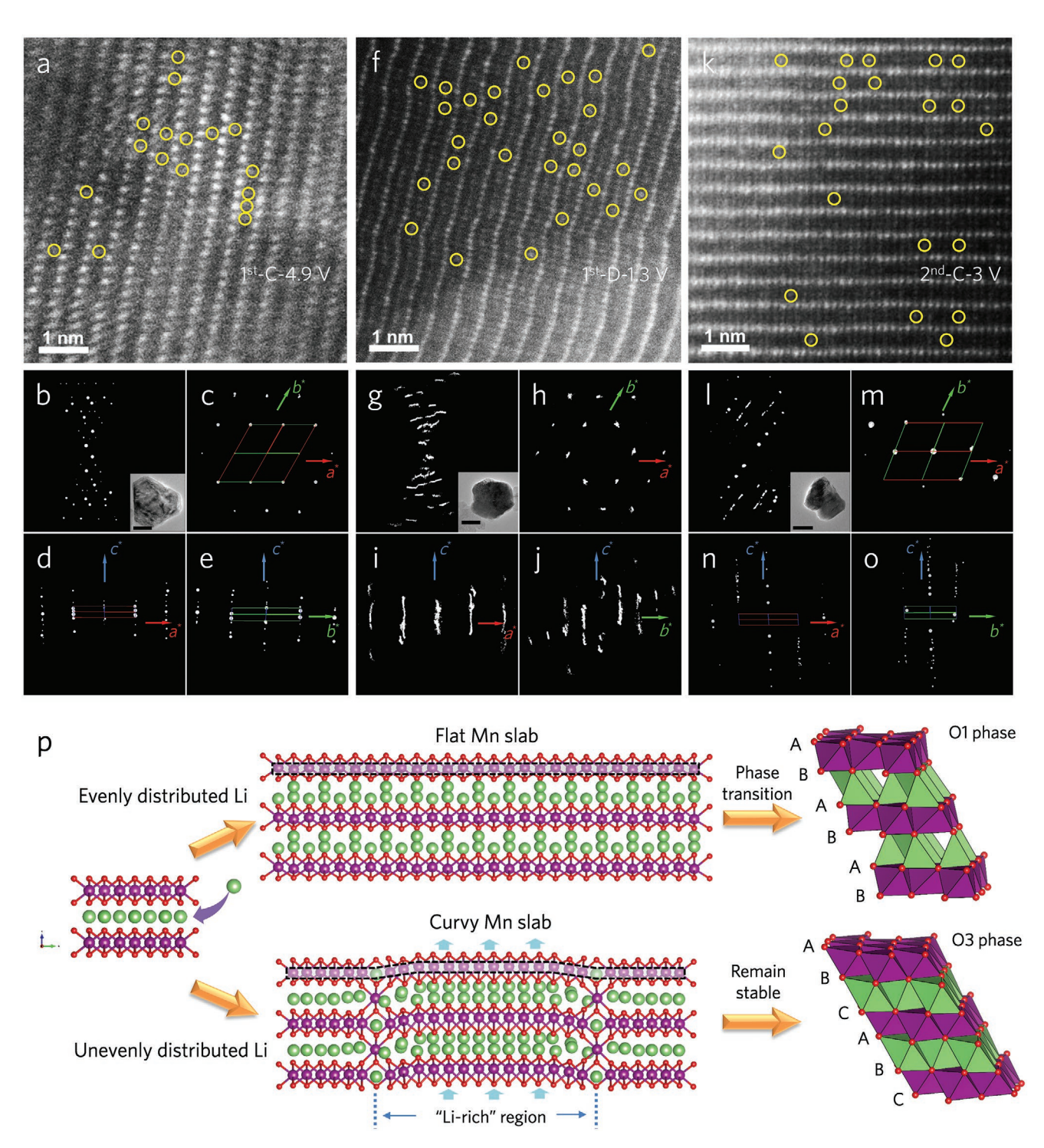


Figure 4. Origin of Structural reversibility in LMO. a,f,k) HAADF-STEM images of LMO after initial charged 4.9 V versus Li/Li⁺, discharged to 1.3 V versus Li/Li⁺ and recharged to 3.0 V versus Li/Li⁺, respectively. Some bright spots representing Mn atoms in Li layers are circled out. b) The overall 3D reciprocal lattice of LMO particles charged 4.9 V versus Li/Li⁺, and c-e) the corresponding reciprocal lattice pattern viewed along c^* -axis, b^* -axis, and a^* -axis, respectively. g) The overall 3D reciprocal lattice of LMO particles discharged 1.3 V versus Li/Li⁺, and h-j) the corresponding reciprocal lattice pattern viewed along c^* -axis, b^* -axis, and a^* -axis, respectively. l) The overall 3D reciprocal lattice of LMO particles recharged 3.0 V versus Li/Li⁺, and m-o) the corresponding reciprocal lattice pattern viewed along c^* -axis, b^* -axis, and a^* -axis, b^* -axis, b

exhibits distorted Mn layer. The proposed model is not only in good accordance with our observations in Figure 4f,g, but also explains the ssNMR results in Figure 2h, where two different

chemical environments for Li⁺ coexist at 1.3 V: the main peak at 740 ppm representing octahedral Li while the new peak at the lower chemical shift attributed to tetrahedral Li stored between

www.advancedsciencenews.com



www.advmat.de

1521405, 2022, 30, Downloaded from https://datanced.oninitibitary.wiley.com/doi/10.1002/adm.aa.02020745 by University Town of Shenzhen, Wiley Online Library on [23/11/1025]. See the Terms and Conditions (https://onlinelibrary.wiley.com/terms-and-conditions) on Wiley Online Library for rules of use; OA articles are governed by the applicable Cerative Commons.

distorted Mn layers. Additionally, it is also calculated that Li/Mn antisites could significantly reduce the formation energy of tetrahedral Li⁺ at various states of discharge (Figure S29 and Table S8, Supporting Information).

3. Conclusion

A new layered oxide cathode purely based on manganese (LMO) is reported, which enables ultrahigh reversible capacities via stabilizing tetrahedral Li-storage for the first time. Contrary to previous studies that mainly focus on suppressing cation disorder, the excellent electrochemical reversibility of LMO can be ascribed to the formation of a cation-disordered structure: upon the initial activation process, a significant amount of Mn ions spontaneously migrate to Li layers and function as supporting structural units to prevent irreversible phase transition and structure collapse caused by tetrahedral Li⁺ insertion. Thus, extra Li⁺ can be reversibly stored in the active tetrahedron sites as the cation-disordered elastic lattice can tolerate the huge lattice change to prevent irreversible phase transformation. This finding not only highlights the potential application of lithium manganese oxides, but also defines a new exciting strategy to fully exploit the capacity potentially held in intercalation-type cathode materials.

4. Experimental Section

Material Synthesis: Li_{0.83}Mn_{0.84}O₂ was synthesized using a three-step process. To begin, MnCO₃ was prepared by a co-precipitation method using stoichiometric amount of 0.1 m Na₂CO₃ and 0.5 m Mn(NO₃)₂·4H₂O aqueous solution. The yield of the MnCO₃ was >90%. Then a solid-state sintering method was employed to prepare the sodic precursor from the mixture of Na₂CO₃, Li₂CO₃, and MnCO₃ in a molar ratio of 0.2:0.15:0.7, which were thoroughly ground and calcined at 700 °C for 20 h. After that, 2 g above precursor was then ground with LiNO₃/LiCl (weight ratio = 0.88:0.12) molten salt in a weight ratio of 1:10 and heated at 280 °C for 6 h to obtain the final LMO product, which was washed with deionized water several times and dried at 120 °C in vacuum. The weight of LMO product was >1.6 g. Li_{0.7}MnO₂ was synthesized by mixing Na₂CO₃ and MnCO₃ in a molar ratio of 0.35:1 and calcinated at 700 °C for 20 h, followed by a similar Li⁺/Na⁺ ion-exchange method.

Determination of Cationic Ordering in TM Layer: Based on the chemical formula of LMO, its fully lithiated formula is Li[Li_{0.16}Mn_{0.84}]O₂, corresponding to 0.48Li[Li_{1/3}Mn_{2/3}]O₂·0.52LiMnO₂. In Li[Li_{1/3}Mn_{2/3}]O₂, its TM layers consist of purely Li@Mn₆, while the TM layers in LiMnO₂ are purely composed of Mn@Mn₆. Therefore, the cationic ordering in Mn layer in LMO can be determined to be 0.48 Li@Mn₆ and 0.52 Mn@Mn₆.

Chemical Prelithiation of Graphite Anode: The electrodes were made by a typical slurry casting method with active materials (graphite), conductive carbon (acetylene black), and binder (PVDF) at a mass ratio of 8:1:1. The slurry was casted onto a Cu foil current collector and dried in a vacuum at 100 °C overnight and cut into disks with a diameter of 12 mm. The reaction solution was prepared by dissolving lithium metal slice in as-prepared 0.5 m 4,4"-dimethylbiphenyl in THF, and stirring vigorously for 1 h at 44 °C in an Ar-filled glove box. The molar ratio of Li: 4,4"-dimethylbiphenyl was fixed to 4:1 to supply an enough amount of Li. Then the graphite anodes were immersed in the reaction solution for appropriate time and temperature. Next the graphite anodes were rinsed with 1.0 m LiPF $_6$ in 1:1:1 (v/v/v) EC/DMC/EMC with 5% FEC electrolyte to quench further reaction between solution and the graphite anodes.

Characterizations: The material morphology was observed by a fieldemission SEM (Carl Zeiss SUPRA@55). The elemental composition was

determined using ICP-AES (Horiba Jobinyvon JY2000-2). The powder XRD data was collected by a Bruker D8 Advance X-ray diffractometer with a Cu-Klpha radiation source (K $_{lpha l}$ = 1.54056 Å, K $_{lpha 2}$ = 1.54439 Å). NPD was measured on high resolution powder diffractometer BT1 at National Institute of Standards and Technology (NIST). The combined structural refinement against the synchrotron XRD and the NPD data was performed using the TOPAS v.5.0 software (Bruker AXS).[52] The HRTEM and cRED results were collected on a JEOL-3200FS field-emission TEM operating at an accelerating voltage of 300 kV with a 60 cm camera length, a minimum collection angle of -30° to 30°, and a OneView CMOS camera (Gatan Inc.). The 3D reciprocal lattice pattern was obtained by combining the collect dataset of a selected particle, then reconstructed and analyzed using REDp software. High-resolution STEM images were obtained using a JEOL ARM-200CF operated at 200 kV. To ensure Z contrast, HAADF images were acquired with inner and outer collection angles of 68 and 280 mrad, respectively. The ⁷Li magic-angle-spinning (MAS) ssNMR experiments were conducted on a Bruker AVANCE-400M NMR spectrometer (9.4 T) with the ⁷Li Larmor frequency of 155.6 MHz using 1.3 mm double-resonance MAS probe. The samples were packed into 1.3 mm MAS rotors in Ar atmosphere and spun at 50 kHz. Then the pjMATPASS (Projection of magic-angle turning phase-adjusted spinning sidebands) measurement was used to eliminate side-band with a $\pi/2$ pulse width of 1.8 μs and a recycle delay of 0.03 s. 1 μs LiCl with the chemical shift at 0 ppm was used as the reference. The structure evolution during the cycling was monitored in situ using the synchrotron high-energy XRD with the wavelength of 0.1173 Å in the 11-ID-C beamline of the advanced photon source (APS) at the Argonne National Laboratory. In situ hard XAS measurements during cycling were performed on the electrodes in transmission mode at beamline 11-ID-C and 20-BM-B of the APS at Argonne National Laboratory. The valence information of related elements was collected by an XPS (Thermo Fisher ESCALab220I-XL). The soft XAS (sXAS) experiments were performed at the Shanghai Synchrotron Radiation Facility, under the storage ring conditions of 3.5 GeV and 220 mA current. The L edge of Mn and the K edge of O sXAS spectra were measured at beamline 02B02 of the SiP·ME2 platform. Beamline 02B02 was a bending magnet beamline, which provided photons with energy range from 50 to 2000 eV. The photon flux was about 1011 photons s-1 and the energy resolving power $E/\Delta E$ was up to 13 000@250 eV. The beam size at the sample was set to 150 μm×50 μm. The spectra were collected using surface-sensitive TEY and bulk-sensitive TFY modes simultaneously at room temperature in an ultrahigh vacuum chamber. The photon energy was calibrated with the spectra of the reference samples MnO, and SrTiO₃, which were measured simultaneously.^[53]

Electrochemical Measurements: The electrochemical performance of the cathode materials was measured using the CR2032-type half cells. Active material, conductive carbon black, and PVDF binder at a weight ratio of 8:1:1 were mixed and stirred thoroughly in the N-methyl-2-pyrrolidone solvent to form the slurry, which was then cast onto the Al foil and dried at 120 °C overnight in vacuum to obtain the cathode electrodes. The coin cell was then assembled in an Ar-filled glove box with Li foil as the anode, Celgard film as the separator, and 1.0 M LiPF₆ in 1:1:1 (v/v/v) EC/DMC/ EMC with 5% FEC as the electrolyte. The LMO||graphite pouch full cell was assembled using a lithiated graphite anode. The loading of LMO in coin cell and pouch cell were 3 and 4 mg cm⁻², respectively. The N/P ratio in pouch cell was 1.2, and the thickness of the electrode was \approx 3 μm . The galvanostatic charge and discharge were conducted on a NEWARE battery test system. The CV was carried out on a Solartron Analytical 1470E electrochemical workstation. The homemade DEMS was used to monitor the in situ gas evolution upon cycling.

Computational Methods: All the calculations were performed using the plane-wave based density functional theory method as implemented in the Vienna ab initio simulation package. [54-57] Projector augmented wave potentials were used to probe valence-core interactions. [58,59] The generalized gradient approximation (GGA) with the Perdew–Burke–Ernzerhof functional was chosen as the exchange correlation potential. [60] A cutoff energy was set as 520 eV and the electronic energy convergence criterion was set at 10⁻⁶ eV. In all the calculations, the Brillouin zone was sampled by Monkhorst–Pack k-point grid with density of at least

15214095, 2022, 30, Downloaded from https://advanced.onlinelibrary.wikey.com/doi/10.1002/adma.202202/45 by University Town Of Shenzhen, Wiley Online Library on [23/11/2025]. See the Terms and Conditions (https://onlinelibrary.wiley.com/terms

and-conditions) on Wiley Online Library for rules of use; OA articles are governed by the applicable Creative Commons

1000/(the number of atoms per cell). In order to correctly characterize the localization of transition-metal d-electrons, the GGA+U method was used to account for the strong correlation in the calculations. $^{[6],62]}$ The values for the Hubbard U parameter for Mn was 4.2 eV. $^{[63]}$ Geometries were optimized until the forces on the atoms were less than 0.02 eV Å $^{-1}$. The spin-polarized calculations were considered in all the calculations. All calculations were performed considering a ferromagnetic ordering of Mn atoms

Intercalation–deintercalation voltages (V) were computed using the Nernst equation, $V = \Delta G/(zF)$, where ΔG is the Gibbs free energy change, F is the Faraday constant and z is the charge that is transferred. The change in the Gibbs free energy is defined as $\Delta G = \Delta E + P\Delta V - T\Delta S$, where P and T are pressure and temperature, respectively, and ΔE , ΔV , and ΔS are the change in internal energy, volume, and entropy respectively. The first-principles calculations were carried out at 0 K and zero pressure. Under these conditions, the Gibbs free energy change is then given by the change in the internal energy, $\Delta G = \Delta E$. Thus, for the lithium deintercalation–intercalation voltage is given by

$$V = -\frac{E(\text{Li}_{x_1} \text{Mn}_{0.83} \text{O}_2) - E(\text{Li}_{x_2} \text{Mn}_{0.83} \text{O}_2) - (x_1 - x_2)E(\text{Li})}{(x_1 - x_2)F}$$
(1)

where $x_1 > x_2$ and $E(\text{Li}_{x_1}\text{Mn}_{0.83}\text{O}_2)$ and $E(\text{Li}_{x_2}\text{Mn}_{0.83}\text{O}_2)$ are the internal energies of the lithiated transition metal oxides, respectively, and E(Li) is the internal energy of metallic sodium. All the internal energies were obtained directly from the first-principles calculations.

To obtain the voltage profiles in the charge/discharge process, all stable phases were needed to be confirmed by comparing the formation energy with respect to stable reference materials. The formation energy is given by

$$E_{f}(\text{Li}_{x}\text{Mn}_{0.83}\text{O}_{2}) = E(\text{Li}_{x}\text{Mn}_{0.83}\text{O}_{2}) - \frac{2x}{3}E(\text{Li}_{1.5}\text{Mn}_{0.83}\text{O}_{2}) - \left(1 - \frac{2x}{3}\right)E(\text{Mn}_{0.83}\text{O}_{2})$$
(2)

where $E(\text{Li}_{1.5}\text{Mn}_{0.83}\text{O}_2)$ and $E(\text{Mn}_{0.83}\text{O}_2)$ are the internal energies of the stable reference materials, respectively. All the phases with partial Li occupancy were investigated while Li ordering was designed by using combinatorics. The formation energies of thermodynamically stable phases compared with the reference materials lie on the convex hull of E_f versus composition x.

Supporting Information

Supporting Information is available from the Wiley Online Library or from the author.

Acknowledgements

W.H., L.Y., and Z.C. contributed equally to this work. The authors acknowledge financial support from the Soft Science Research Project of Guangdong Province (2017B030301013), National Key R&D Program of China (2020YFB0704500), Natural Science Foundation of China (Grants No. 11227902), and the Australian Research Council (ARC) (DP200100365, LP180100722).

Conflict of Interest

The authors declare no conflict of interest.

Data Availability Statement

The data that support the findings of this study are available from the corresponding author upon reasonable request.

Keywords

elastic lattices, layered oxide cathodes, Li-ion batteries, reversible tetrahedral sites, ultrahigh capacity

Received: March 24, 2022 Revised: June 2, 2022 Published online: June 23, 2022

- [1] J. R. Owen, Chem. Soc. Rev. 1997, 26, 259.
- [2] J. Zheng, Y. Ye, T. Liu, Y. Xiao, C. Wang, F. Wang, F. Pan, Acc. Chem. Res. 2019, 52, 2201.
- [3] L. Yang, K. Yang, J. Zheng, K. Xu, K. Amine, F. Pan, Chem. Soc. Rev. 2020, 49, 4667.
- [4] J. Zheng, Y. Ye, F. Pan, Natl. Sci. Rev. 2019, 2, 242.
- [5] K. Kang, C. H. Chen, B. J. Hwang, G. Ceder, Chem. Mater. 2004, 16, 2685
- [6] J. R. Dahn, U. von Sacken, C. A. Michal, Solid State Ionics 1990, 44, 87.
- [7] R. Robert, P. Novák, Chem. Mater. 2018, 30, 1907.
- [8] I. Davidson, J. E. Greedan, U. von Sacken, C. A. Michal, J. R. Dahn, Solid State Ionics 1991, 46, 243.
- [9] G. Assat, J. M. Tarascon, Nat. Energy 2018, 3, 373.
- [10] W. Wei, L. Chen, A. Pan, D. G. Ivey, Nano Energy 2016, 30, 580.
- [11] K. Luo, M. R. Roberts, R. Hao, N. Guerrini, E. Liberti, C. S. Allen, A. I. Kirkland, P. G. Bruce, *Nano Lett.* 2016, 16, 7503.
- [12] H. Zheng, Z. Hu, P. Liu, W. Xu, Q. Xie, W. He, Q. Luo, L. Wang, D. D. Gu, B. Qu, Z. Z. Zhu, D. L. Peng, Energy Storage Mater. 2020, 25, 76.
- [13] D. Eum, B. Kim, S. J. Kim, H. Park, J. Wu, S. P. Cho, G. Yoon, M. H. Lee, S. K. Jung, W. Yang, W. M. Seong, K. Ku, O. Tamwattana, S. K. Park, I. Hwang, K. Kang, Nat. Mater. 2020, 19, 419.
- [14] X. D. Zhang, J. L. Shi, J. Y. Liang, Y. X. Yin, J. N. Zhang, X. Q. Yu, Y. G. Guo, Adv. Mater. 2018, 30, 1801751.
- [15] R. A. House, L. Jin, U. Maitra, K. Tsuruta, J. W. Somerville, D. P. Förstermann, F. Massel, L. Duda, M. R. Roberts, P. G. Bruce, Energy Environ. Sci. 2018, 11, 926.
- [16] Y. Zuo, B. Li, N. Jiang, W. Chu, H. Zhang, R. Zou, D. Xia, Adv. Mater. 2018, 30, 1707255.
- [17] Z. Zhuo, K. Dai, R. Qiao, R. Wang, J. Wu, Y. Liu, J. Peng, L. Chen, Y. de Chuang, F. Pan, Z. xun Shen, G. Liu, H. Li, T. P. Devereaux, W. Yang, Joule 2021, 5, 975.
- [18] Z. Zhuo, K. Dai, J. Wu, L. Zhang, N. Tamura, Y. De Chuang, J. Feng, J. Guo, Z. X. Shen, G. Liu, F. Pan, W. Yang, ACS Energy Lett. 2021, 3. 3417.
- [19] X. Cao, H. Li, Y. Qiao, M. Jia, X. Li, J. Cabana, H. Zhou, Adv. Mater. 2021, 33, 2004280.
- [20] J. Song, B. Li, Y. Chen, Y. Zuo, F. Ning, H. Shang, G. Feng, N. Liu, C. Shen, X. Ai, D. Xia, Adv. Mater. 2020, 32, 2000190.
- [21] H. Shang, Y. Zuo, F. Shen, J. Song, F. Ning, K. Zhang, L. He, D. Xia, Nano Lett. 2020, 20, 5779.
- [22] W. Huang, C. Lin, J. Qiu, S. Li, Z. Chen, H. Chen, W. Zhao, G. Ren, X. Li, M. Zhang, F. Pan, Chem 2022, https://doi.org/10.1016/j. chempr.2022.04.012.
- [23] K. Redel, A. Kulka, A. Plewa, J. Molenda, J. Electrochem. Soc. 2019, 166, A5333.
- [24] K. A. Jarvis, Z. Deng, L. F. Allard, A. Manthiram, P. J. Ferreira, Chem. Mater. 2011, 23, 3614.
- [25] M. Freire, N. V. Kosova, C. Jordy, D. Chateigner, O. I. Lebedev, A. Maignan, V. Pralong, Nat. Mater. 2016, 15, 173.
- [26] R. Kataoka, N. Taguchi, T. Kojima, N. Takeichi, T. Kiyobayashi, J. Mater. Chem. A 2019, 7, 5381.

15214095, 2022, 30, Downloaded from https://advanced.onlinelibrary.wiley.com/doi/10.1002/adma.202202745 by University Town Of Shenzhen, Wiley Online Library on [23/11/2025]. See the Terms

and Conditions (https://onlinelibrary.wiley.com/term:

for rules of use; OA

articles are governed by the applicable Creative Commons

- [27] J. Lee, D. A. Kitchaev, D. Kwon, C. Lee, J. K. Papp, Y. Liu, Z. Lun, R. J. Clément, T. Shi, B. D. Mccloskey, J. Guo, M. Balasubramanian, G. Ceder, *Nature* 2018, 556, 185.
- [28] Z. Lun, B. Ouyang, Z. Cai, R. J. Clément, D.-H. Kwon, J. Huang, J. K. Papp, M. Balasubramanian, Y. Tian, B. D. McCloskey, H. Ji, H. Kim, D. A. Kitchaev, G. Ceder, Chem 2020, 6, 153.
- [29] H. Ji, J. Wu, Z. Cai, J. Liu, D. H. Kwon, H. Kim, A. Urban, J. K. Papp, E. Foley, Y. Tian, M. Balasubramanian, H. Kim, R. J. Clément, B. D. McCloskey, W. Yang, G. Ceder, *Nat. Energy* 2020, 5, 213.
- [30] W. Yin, A. Grimaud, G. Rousse, A. M. Abakumov, A. Senyshyn, L. Zhang, S. Trabesinger, A. Iadecola, D. Foix, D. Giaume, J. M. Tarascon, *Nat. Commun.* 2020, 11, 1252.
- [31] Y. Lyu, N. Zhao, E. Hu, R. Xiao, X. Yu, L. Gu, X. Q. Yang, H. Li, Chem. Mater. 2015, 27, 5238.
- [32] Y. Lyu, E. Hu, D. Xiao, Y. Wang, X. Yu, G. Xu, S. N. Ehrlich, K. Amine, L. Gu, X. Q. Yang, H. Li, Chem. Mater. 2017, 29, 9053.
- [33] T. Sato, K. Sato, W. Zhao, Y. Kajiya, N. Yabuuchi, J. Mater. Chem. A 2018, 6, 13943.
- [34] M. Tian, Y. Gao, Z. Wang, L. Chen, Phys. Chem. Chem. Phys. 2016, 18, 17345.
- [35] G. Liang, C. Didier, Z. Guo, W. K. Pang, V. K. Peterson, Adv. Mater. 2020, 32, 1904528.
- [36] J. Li, C. Lin, M. Weng, Y. Qiu, P. Chen, K. Yang, W. Huang, Y. Hong, J. Li, M. Zhang, C. Dong, W. Zhao, Z. Xu, X. Wang, K. Xu, J. Sun, F. Pan, Nat. Nanotechnol. 2021, 16, 599.
- [37] J. Choi, H. Jeong, J. Jang, A. R. Jeon, I. Kang, M. Kwon, J. Hong, M. Lee, J. Am. Chem. Soc. 2021, 143, 9169.
- [38] J. Zheng, P. Xu, M. Gu, J. Xiao, N. D. Browning, P. Yan, C. Wang, J. G. Zhang, Chem. Mater. 2015, 27, 1381.
- [39] M. Gu, I. Belharouak, J. Zheng, H. Wu, J. Xiao, A. Genc, K. Amine, S. Thevuthasan, D. R. Baer, J. G. Zhang, N. D. Browning, J. Liu, C. Wang, ACS Nano 2013, 7, 760.
- [40] C. S. Johnson, J. S. Kim, A. Jeremy Kropf, A. J. Kahaian, J. T. Vaughey, M. M. Thackeray, Electrochem. Commun. 2002, 4, 492.
- [41] C. P. Grey, N. Dupré, Chem. Rev. 2004, 104, 4493.
- [42] M. Jiang, B. Key, Y. S. Meng, C. P. Grey, Chem. Mater. 2009, 21, 2733.

- [43] C. Pan, Y. J. Lee, B. Ammundsen, C. P. Grey, Chem. Mater. 2002, 14, 2289.
- [44] S. Zheng, F. Zheng, H. Liu, G. Zhong, J. Wu, M. Feng, Q. Wu, W. Zuo, C. Hong, Y. Chen, K. An, P. Liu, S. Wu, Y. Yang, ACS Appl. Energy Mater. 2019, 2, 5933.
- [45] X. Li, Y. Qiao, S. Guo, Z. Xu, H. Zhu, X. Zhang, Y. Yuan, P. He, M. Ishida, H. Zhou, Adv. Mater. 2018, 30, 2.
- [46] R. A. House, U. Maitra, M. A. Pérez-Osorio, J. G. Lozano, L. Jin, J. W. Somerville, L. C. Duda, A. Nag, A. Walters, K. J. Zhou, M. R. Roberts, P. G. Bruce, *Nature* 2020, 577, 502.
- [47] P. Yan, J. Zheng, Z.-K. Tang, A. Devaraj, G. Chen, K. Amine, J.-G. Zhang, L.-M. Liu, C. Wang, Nat. Nanotechnol. 2019, 14, 602.
- [48] W. Huang, C. Lin, M. Zhang, S. Li, Z. Chen, W. Zhao, C. Zhu, Q. Zhao, H. Chen, F. Pan, Adv. Energy Mater. 2021, 11, 2102646.
- [49] A. Fasolino, J. H. Los, M. I. Katsnelson, Nat. Mater. 2007, 6, 858.
- [50] P. Kumar, K. V. Agrawal, M. Tsapatsis, K. A. Mkhoyan, *Nat. Commun.* 2015, 6, 7128.
- [51] X. Lu, Y. Sun, Z. Jian, X. He, L. Gu, Y. S. Hu, H. Li, Z. Wang, W. Chen, X. Duan, L. Chen, J. Maier, S. Tsukimoto, Y. Ikuhara, *Nano Lett.* 2012, 12, 6192.
- [52] A. A. Coelho, J. Appl. Crystallogr. 2018, 51, 210.
- [53] G. Ren, N. Zhang, X. Feng, H. Zhang, P. Yu, S. Zheng, D. Zhou, Z. Tian, X. Liu, Chin. Phys. B 2020, 29, 016101.
- [54] G. Kresse, J. Hafner, Phys. Rev. B 1993, 47, 558.
- [55] G. Kresse, J. Furthmüller, Comput. Mater. Sci. 1996, 6, 15.
- [56] G. Kresse, J. Furthmüller, Phys. Rev. B: Condens. Matter Mater. Phys. 1996, 54, 11169.
- [57] S. K. Mishra, G. Ceder, Phys. Rev. B: Condens. Matter Mater. Phys. 1999, 59, 6120.
- [58] P. E. Blöchl, Phys. Rev. B 1994, 50, 17953.
- [59] D. Joubert, Phys. Rev. B: Condens. Matter Mater. Phys. 1999, 59, 1758.
- [60] J. P. Perdew, K. Burke, M. Ernzerhof, Phys. Rev. Lett. 1996, 77, 3865.
- [61] S. Dudarev, G. Botton, Phys. Rev. B: Condens. Matter Mater. Phys. 1998, 57, 1505.
- [62] V. I. Anisimov, J. Zaanen, O. K. Andersen, Phys. Rev. B 1991, 44, 943.
- [63] L. Wang, T. Maxisch, G. Ceder, Chem. Mater. 2007, 19, 543.